Nano Energy 120 (2024) 109105

Contents lists available at ScienceDirect

Nano Energy

journal homepage: www.elsevier.com/locate/nanoen

Light-emitting MOS junction for ultrahigh-resolution quantum dot displays

Junlong Li [a,1], Jiawen Qiu [a,1], Biao Xie [a], Wenhao Li [a], Kun Wang [a], Chan Hee Suk [c], Chaoxing Wu [a,b,*], Yongshen Yu [b], Yun Ye [a,b], Xiongtu Zhou [a,b,*], Yongai Zhang [a,b,*], Tailiang Guo [a,b], Tae Whan Kim [c,**]

[a] College of Physics and Information Engineering, Fuzhou University, Fuzhou 350108, China
[b] Fujian Science & Technology Innovation Laboratory for Optoelectronic Information of China, Fuzhou 350108, China
[c] Department of Electronic and Computer Engineering, Hanyang University, Seoul 04763, Republic of Korea

ARTICLE INFO

Keywords:
Quantum dot
Light-emitting device
High resolution
MOS junction
Display

ABSTRACT

A high-resolution quantum-dot (QD) light-emitting device array is considered to be the key component in a high resolution near-eye micro-display. Although much research has been committed to the achievement of a high-resolution QD pattern, realizing a sub-10 micrometer or even a sub-micrometer device array is challenging because of the requirement for precise vertical multilayer alignment and the existence of electric-crosstalk effects. In this work, we propose a QD-based light-emitting metal/oxide/semiconductor junction (LE-MOSJ) with a super-simple structure of ITO/Al_2O_3/QDs/Ag with no injection or transfer layer. We measured the voltage-frequency-electroluminescence, spectrum-voltage, and spectrum-frequency characteristics, used voltage-dependent time-resolved electroluminescence to analyze the carrier transport behavior and the working mechanism, and attribute the electron source for the electroluminescence to free and surface defect-captured electrons. Finally, we successfully demonstrate an ultrahigh-resolution LE-MOSJ array with ~4200 pixels per inch (PPI). We believe the proposed LE-MOSJ can provide an optional approach for realizing ultrahigh-resolution QD-based display technology.

1. Introduction

With the advent of the Internet of Things, fifth-generation mobile networks, and artificial intelligence, which set higher standards for display technology such as ultrahigh resolution, longer lifetime and wider color gamut, near-eye displays are now considered to be examples of next-generation display technology [1,2]. Among the display parameters, ultrahigh resolution is particularly important because high resolution can close the gap between real world and display images for a more realistic visual experience. Therefore, various micro-display technologies, including gallium nitride-based micro-light-emitting diodes (Micro-LEDs), organic materials-based micro-organic light-emitting diodes (Micro-OLEDs), and liquid crystal-based micro--liquid crystal on silicon (Micro-LCoS), have emerged as potential candidates for use in near-eye displays [3–5]. However, as the size of the light-emitting device (pixel) downscales, the performance of the light emission from a Micro-LED/Micro-OLED decreases as does the light modulation from a Micro-LCoS. As a result, realizing sub-10 micrometer, or even sub-micrometer, pixel size is challenging.

Colloidal quantum dots (QDs) have emerged as a high-quality photonic and electronic nanomaterial for display applications due to their having tunable emission color, wide color gamut, and high color purity [6–10]. Especially, QDs are promising for realizing ultrahigh-resolution near-eye displays with sub-10 micrometer, or even sub-micrometer, pixel size because, in theory, QD clusters, and even a single QD (less than 10 nm), have excellent electroluminescence characteristics [11,12], which can fully meet the requirements of ultrahigh-resolution displays with sub-10 micrometer, or even sub-micrometer, pixel size.

Achieving ultrahigh-resolution luminescence from a pixel array through the patterning of QD layers has been extensively explored, and inkjet printing, transfer printing, and photolithography are the best ways to do so [13–21]. Inkjet printing is regarded as the most promising technique for manufacturing large-area, low-cost patterned QD layers. Especially, electrohydrodynamic (EHD) printing technology provides a

* Corresponding authors at: College of Physics and Information Engineering, Fuzhou University, Fuzhou 350108, China.
** Corresponding author.
E-mail addresses: chaoxing_wu@fzu.edu.cn (C. Wu), xtzhou@fzu.edu.cn (X. Zhou), yongaizhang@fzu.edu.cn (Y. Zhang), twk@hanyang.ac.kr (T.W. Kim).
[1] Both authors contributed equally to this work.

https://doi.org/10.1016/j.nanoen.2023.109105
Received 4 September 2023; Received in revised form 17 October 2023; Accepted 15 November 2023
Available online 18 November 2023

feasible solution for manufacturing high-resolution pixelated QDs. In 2020, Yin et al. employed EHD and a mixed solvent method to fabricate successfully a QD matrix with a 1-μm diameter and 306 pixels per inch (PPI) [22]. In contrast to inkjet print, transfer printing is a contact method that can be used to fabricate nanoscale-patterned QD layers simply and efficiently. Qian et al. used PDMS stamps to manufacture an ultrahigh-resolution red QD-LED [23]. Moreover, photolithography has advantages when developing large-area and precisely patterned QD layers. In 2022, Bea et al. used a dual-ligand passivation system to devise QDs comprising photocrosslinkable and dispersing ligands [24], and RGB QD patterns with resolutions up to 15000 PPI can be obtained by manipulating the ligands.

Although the patterning of QD layers is considered as a key step for achieving high-resolution QD-LEDs, few studies have concentrated on the patterning of the functional layers, including the electron/hole injection layers and transfer layers, and most of the reported high-resolution QD-LEDs use non-patterned functional layers. Typically, electroluminescence (EL) from QD-LEDs is obtained due to radiative recombination of electrons and holes injected from external electrodes [25–27]. Therefore, precisely designed band matching to ensure a balance between electrons and holes injection is necessary, leading to the introduction of diverse organic/inorganic functional layers for energy-level modification [10]. However, the complex multilayer organic/inorganic functional layers make the miniaturization of pixels

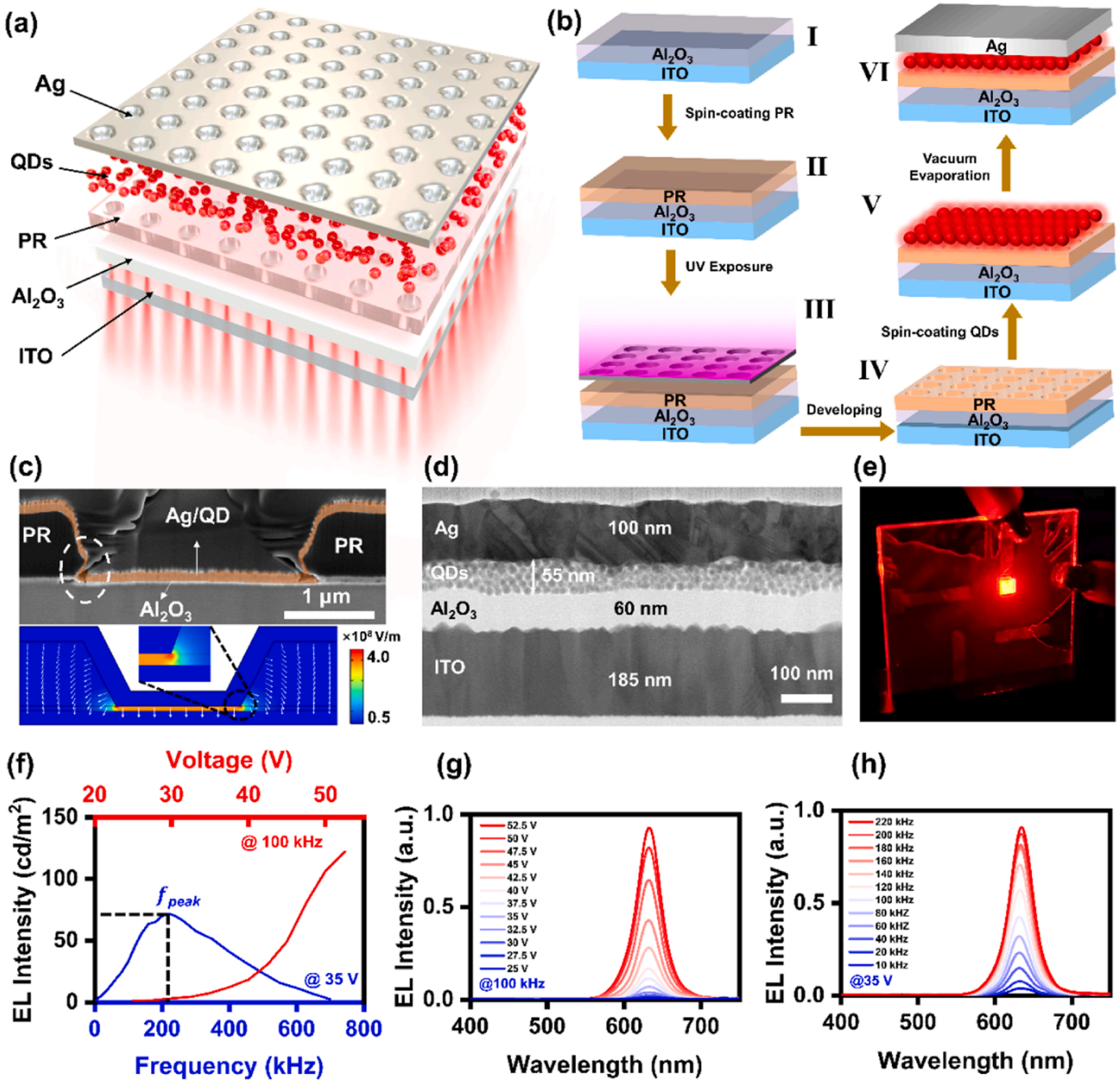

Fig. 1. Structure and optical-electrical properties of the LE-MOSJ array. (a) Schematic structure of the LE-MOSJ array. (b) Schematic description of the fabrication of the LE-MOSJ array. (c) Cross-sectional SEM image of the LE-MOSJ (top) and simulated electric field distribution (bottom). (d) Cross-sectional TEM image of the LE-MOSJ. (e) Photograph of the operating LE-MOSJ array. (f) EL-voltage relationship at a frequency of 100 kHz and EL-frequency relationship at a voltage of 35 V. (g) EL spectra-voltage relationship at a frequency of 100 kHz. (h) EL spectra-frequency relationship at a voltage of 35 V.

difficult. Especially, it can be expected that the realization of precise vertical alignment of the multi-layers on a micro/nano scale is difficult. Therefore, the reported works about high-resolution QD-LED just demonstrate the realization of patterned QD layer [14]. Additionally, when the pixel interval is reduced to a sub-micrometer level for application in ultrahigh-resolution displays, electrical isolation from neighboring pixels is challenging due to the conductance of the semiconductor layer. As a result, it is possible that voltage applied to a selected pixel will also drive the electrons/holes in neighboring unselected pixels, resulting in electric crosstalk [28–30].

In order to avoid the need for precise vertical alignment and to overcome the effect of electric crosstalk in ultrahigh-resolution displays, we present a QD-based light-emitting metal/oxide/semiconductor junction (LE-MOSJ), which has a super-simple structure with no electron/hole injection layer or transfer layer. The LE-MOSJ is only composed of electrodes, an insulator, and a QD layer and has an ultra-simple structure of indium tin oxide/Al_2O_3/QDs/Ag. We measure the photoelectric characteristics of the device, such as its voltage-frequency-EL intensity, the EL-spectrum voltages, and the EL-spectrum frequencies, and we use voltage-dependent time-resolved EL to analyze the carrier transport behavior and the working mechanism. We attribute the electron source for the electroluminescence to free and defect-captured electrons, which leads to two temporally separated EL peaks during the switching of the voltage polarity. Finally, we use photolithography technology to fabricate an ultrahigh-resolution LE-MOSJ array with ~4200 PPI and discover that the natural fringe effect decreases the operation voltage. Based on the data presented in this paper, we suggest that our proposed LE-MOSJ can provide an optional approach for realizing ultrahigh-resolution QD-based displays.

2. Result and discussion

The LE-MOSJ is composed of only an indium-tin-oxide (ITO) electrode, an Al_2O_3 insulator, a CdSe/ZnS QD layer, and an Ag electrode, forming a MOS structure. As is well known, colloidal CdSe/ZnS QDs exhibit high efficiency and stability, and are widely used in conventional QD-LEDs. Therefore, CdSe/ZnS QDs are selected as the light-emitting layer in this work. To fabricate the high-resolution LE-MOSJ array, we employed a patterned photoresist (PR), as schematic illustrated in Fig. 1 (a). Fig. 1(b) presents the fabrication process for the LE-MOSJ array. Firstly, an Al_2O_3 layer is deposited on ITO electrodes by using atomic layer deposition (ALD) (Fig. 1b-I). Then, the PR layer with an array of holes (3 μm in diameter, 6 μm in pitch) is obtained by using photolithography (Fig. 1b-II, b-III, and 1b-IV). CdSe/ZnS QDs are then spin-coated onto a patterned PR layer (Fig. 1b-V), and finally, Ag electrodes are deposited by using thermal evaporation (Fig. 1b-VI). The reader should note that the patterned PR layer plays two roles: (1) it is used as a mask to realize a high-resolution QD pattern, and (2) its fringe effect causes a decrease in the operation voltage. As an equipotential body, the maximum surface electric field of the Ag film can be obtained in the location where the radius of curvature reaches its minimum value. Therefore, the highest electric field can be obtained in the PR-Ag-Al_2O_3 contact, namely, the fringe effect, as indicated by the white circle in Fig. 1(c). The top panel in Fig. 1(c) shows a cross-sectional scanning electron microscope (SEM) image of the device, where the Ag film fully covers the patterned PR layer. To confirm the fringe effect, we built a finite-element simulation model of the device, as shown in the bottom panel of Fig. 1(c), and we found that the highest electric field was obtained at the edge of the PR layer, as indicated by the blue circle.

A cross-sectional transmission electron microscope (TEM) image of the LE-MOSJ is shown in Fig. 1(d). An Al_2O_3 insulating layer (60-nm thick) is introduced between the bottom ITO electrode and the QD layer (55-nm thick) to completely suppress external carrier injection from the ITO [31–33]. The Ag electrode is directly deposited on the top surface of the QD layer. Thus, charge carriers can only be injected into the QDs from the Ag electrode. If stable electroluminescence is to be realized, an AC driving voltage is necessary. Upon application of a sinusoidal voltage (50 V, 100 kHz) to the LE-MOSJ, the device is observed to have an EL intensity of 106.5 cd/m^2, as shown in Fig. 1(e). The size of the light-emitting area is 2 mm × 2 mm.

Because the structure and the driving mode of the LE-MOSJ will be different from those of conventional QD-LEDs, we measured the opto-electronic characteristics of the device. We define the turn-on voltage as the voltage amplitude at which an EL intensity of 1 cd/m^2 is observed. As shown in Fig. 1(f), the turn-on voltage is approximately 25 V at a frequency of 100 kHz. When the amplitude of the voltage exceeds the turn-on voltage, the EL intensity increases exponentially with increasing voltage (red line in Fig. 1(f)). In conventional QD-LEDs, the luminescence of the device mainly depends on the driving voltage and the injected current. However, the EL intensity of the LE-MOSJ is not only related to the amplitude of the voltage, but also sensitively to the frequency of the voltage [34,35]. Typically, as the frequency increases, the EL intensity increases to a maximum value and then decreases (blue line at Fig. 1(f)). The frequency corresponding to the maximum EL intensity is defined as f_{peak}. Before f_{peak} is reached, the EL intensity increases with increasing frequency due to an increase in the number of light pulses per unit time. However, when the frequency is higher than f_{peak}, the EL intensity of the device decreases because electrons and holes have less time to participate in radiative recombination due to the short driving period, and the carriers are then pulled apart by the subsequent reverse electric field. To further reveal the emission properties of the devices, we measured EL spectra under different voltages and frequencies, and the results are shown in Fig. 1(g) and (h). Especially, in order to ensure the stability of the devices and the accuracy of the results, we measure the EL spectra-voltage relationship at a frequency of 100 kHz and the EL spectra-frequency relationship at a voltage of 35 V. The EL intensity increases with increasing amplitude of the driving voltage from 25 V to 52.5 V. Additionally, when the driving frequency is below f_{peak}, the EL intensity also increases with increasing driving frequency from 10 kHz to 220 kHz. As the voltage and the frequency change, the central wavelength of the EL is barely shifted, indicating high color stability.

In conventional QD-LEDs, electrons and holes are continuously injected into the device from the external electrodes. Different from the conventional mode, electrons and holes are periodically injected from the Ag electrode in our LE-MOSJ device. Generally speaking, holes are injected during the positive half cycle and electrons are injected during the negative half cycle. However, the detailed carrier injection process is unclear. Therefore, we investigated the carrier transport behaviors through time-resolved EL to provide a clear physical image for the working mechanism. In this measurement, a square-wave voltage (42.5 V, 40 kHz) was applied to the Ag electrode, and the ITO electrode was grounded. As shown in Fig. 2(a) and (b), four luminescence peaks appear in one voltage cycle, which is different from conventional light-emitting devices. When the voltage is switched from a positive to a negative half cycle (Fig. 2(a)), a luminescence peak with a small amplitude appears (defined as P1), followed by a luminescence peak with a larger amplitude (defined as P2). In contrast, when the voltage is switched from a negative to a positive half cycle (Fig. 2(b)), a strong luminescence peak occurs first (defined as P3), followed by a weak luminescence peak (defined as P4).

As is well known, the intensity and the phase of EL peaks reflect the distribution and the transport of charge carriers [36]. The existence of two temporally separated EL peaks during the voltage polarity switching process shows that if EL is to be realized, two electron sources are needed. Additionally, the transition time from the electron sources to the QD luminescence center varies. Therefore, the time-resolved EL characteristics of devices under different voltages are studied to observe the carrier transport behavior, as shown in Fig. 2(c). The EL intensities of the four peaks under different voltages are extracted, as shown in Fig. 2 (d). Generally, the intensities of the four luminescent peaks increase with increasing voltage, because as the voltage increases, more carriers will be injected into the QDs for radiative recombination. Noting that

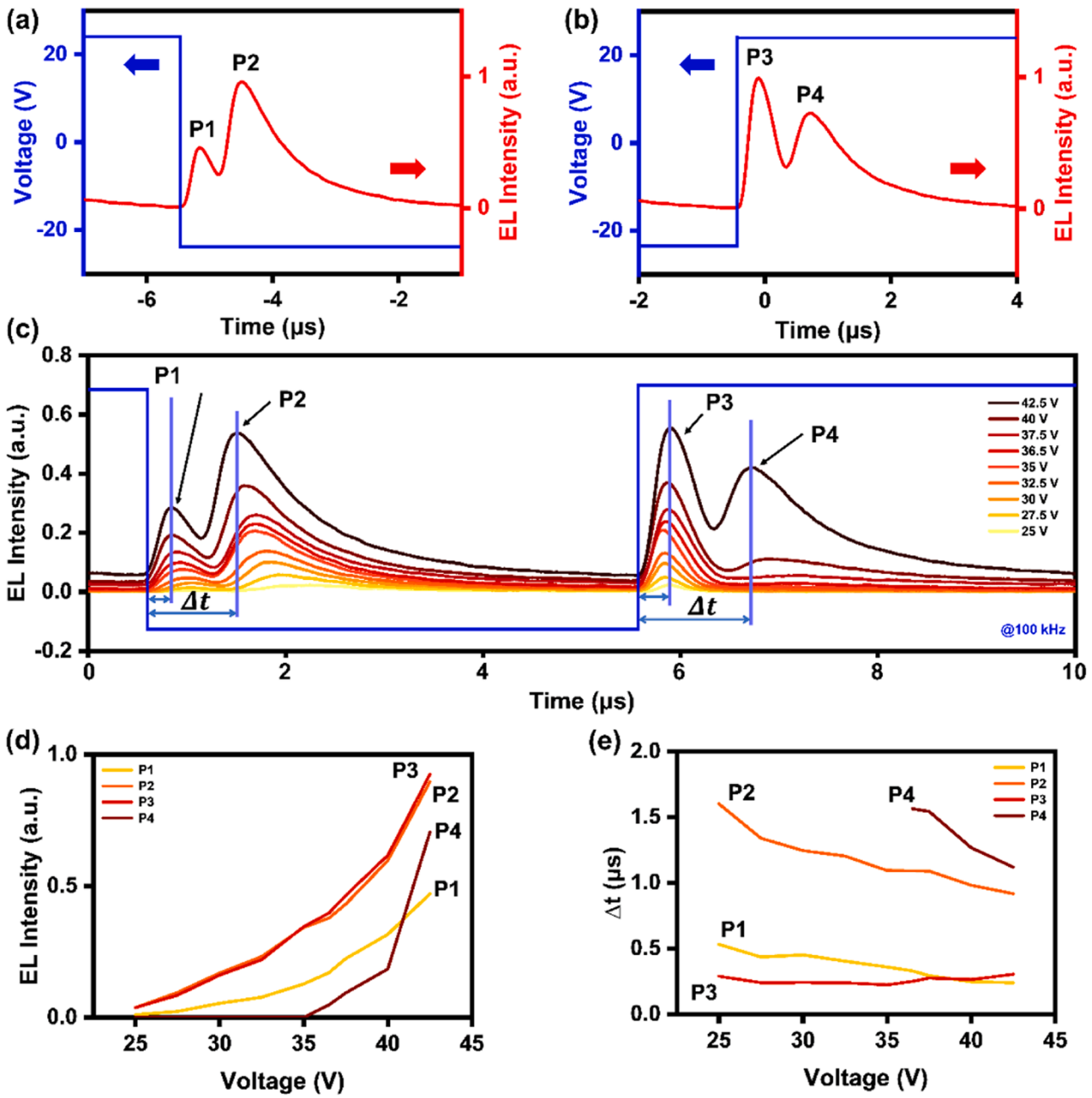

Fig. 2. Time-resolved EL characteristics of the LE-MOSJ array. Time-resolved EL when the voltage switches (a) from positive to negative and (b) from negative to positive. (c) Time-resolved EL under different voltage when the voltage polarity is switching. (d) Variations of the EL intensity and (e) Δt under different voltages.

with increasing voltage, the luminescence intensity of P2 is always higher than that of P1 and P2 increases faster than P1, which indicates that the electron source contributing to P2 is more sensitive to voltage and the electron source contributing to P2 can provide more electrons.

Similarly, when the voltage is switched from negative bias to positive bias, the luminescence intensity of P4 increases more rapidly than that of P3, demonstrating that the electron source supplying electrons to P4 is more sensitive to the voltage. However, the luminescence intensity of P4 is always smaller than that of P3, implying that the electron source for P4 provides fewer electrons than that for P3. Worth noting is that P4 appears only at high voltages ($>$ 35 V), suggesting that the electron source contributing to P4 cannot provide electrons at low voltages.

In addition, the time interval between the appearance of the luminescence peak and the voltage jump (defined as Δt) is presented in Fig. 2 (e). The phase of each luminescence peak is influenced by the voltage, showing that the electron transit process (from the electron source to the QD luminescence center) is obviously influenced by the voltage. The values of Δt for P2 and P4 are always larger than those for P1 and P3. Moreover, the electron sources contributing to P2 and P4 are greatly influenced by the electric field. Therefore, the types of electron sources contributing to P2 and P4 are totally different from those contributing to P1 and P3. Moreover, P4 appears only at high voltages and its Δt decreases faster than P2. Therefore, the electron source contributing to P4 is also a little different from that contributing to P2, which will be discussed later.

The electroluminescent characteristics come from the asymmetric structure of the LE-MOSJ (one side has an ITO/Al_2O_3/QD structure; the other side has a QD/Ag structure). Based on the above experimental results and analysis, we tend to attribute the four luminescence peaks to the following electron sources: (1) the electrons contributing to P1 are

those injected directly into the QDs from the Ag electrode; (2) the electrons contributing to P2 are those trapped by shallow defects at the Ag/QD interface; (3) the electrons contributing to P3 are those that electrically accumulate at the Al_2O_3/QD interface; (4) the electrons contributing to P4 are those trapped by shallow defects at the Al_2O_3/QD interface. Moreover, the difference between the shallow defects at the Ag/QD interface and the Al_2O_3/QD interface leads to an obvious difference between the P2 and the P4 luminescence peaks. As for the formation of Ag/QD interface, the Ag film is deposited on the QD layer by using the thermal evaporation. The intense thermal evaporation of Ag will destroy the surface ligands of the QDs and introduce more defects at the Ag/QD interface. However, for the formation of Al_2O_3/QD interface, the QDs are spin-coated on the Al_2O_3 layer. Therefore, the Al_2O_3/QD interface has less defects than the Ag/QD interface. The four EL peaks are summarized in Table 1 as follows:

To confirm whether more defects will be introduced into the Ag/QD interface during the thermal evaporation, we adopted a variety of characterization methods. We analyzed the difference between the Ag/QD interface and the Al_2O_3/QD interface by using cross-sectional TEM, and the result is shown in Fig. 3(a). QDs are clearly seen in the Al_2O_3/QD interface while the QDs at the Ag/QD interface are very fuzzy, indicating that Ag atoms have fully permeated into the surface of the QD film. Furthermore, magnified images of the QD films at the interfaces are presented in Fig. 3(b). The Ag atoms are found to fill the nanogaps between QDs and gradually to fuse with the QDs at the Ag/QD interface (top panel in Fig. 3(b)). Therefore, the surface ligands of the QDs may have been destroyed, causing several defects at the Ag/QD interface. However, the Al_2O_3/QD interface is observed obviously to have a sharp edge (bottom panel in Fig. 3(b)), so the surface state of the QD film will be preserved to a greater extent, leaving fewer defects at that interface.

To verify the above speculation that the thermal evaporation of Ag will introduce defects at the surface of the QD film, we studied the fluorescence characteristics of the QD film before and after the thermal evaporation of Ag. Fig. 3(c) shows the room-temperature, temporal evolution of the two types of devices, one with and the other without Ag. The fluorescent lifetime of the QD film (QDs/Al_2O_3/ITO) is seen to be shorter after the thermal evaporation of Ag (from 15.64 to 9.55 ns), which indicates that defects at the Ag/QD interface can provide an additional decay channel for excitons. In addition, the photoluminescence (PL) spectra of the two samples are also measured, and the result is shown in Fig. 3(d). The intensity of the PL peak of the sample without Ag is higher than that of the PL peak of the sample with Ag. This could be due to non-radiative transitions occurring at the Ag/QD interface and causing a relatively low fluorescence quantum yield [37,38]. Those results show that more defects are generated in the process of Ag evaporation and that more defects are present at Ag/QD interface than at the Al_2O_3/QD interface, as shown in Fig. 3(e).

To simplify the model, we consider only the motion of electrons. The three stages (I, II, III) in Fig. 4(a) are used to illustrate the transport of electrons when the voltage switches from positive to negative. Similarly, the three stages (IV, V, VI) in Fig. 4(b) are used to illustrate the transport of electrons when the voltage switches from negative to positive. In the positive half-cycle of the square-wave voltage (stage I), electrons accumulate in the ITO/Al_2O_3 interface in the initial state, as shown in Fig. 4(c)-I. When the applied voltage switches from positive to negative (stage II), electrons are injected into the device from the Ag electrode through an external circuit. Due to the large number of traps at the Ag/QD interface, most of the electrons are trapped and cannot move to the QDs. As a result, only a few electrons are transported to the QDs, so a luminescence peak (P1) with a smaller amplitude is generated, as illustrated in Fig. 4(c)-II. As time goes by (stage III), trapped electrons are gradually released and transported to the QDs under an external electric field to take part in radiative recombination, so a luminescence peak (P2) with a larger amplitude is generated, as illustrated in Fig. 4(c)-III. That more carriers are injected into the device and engage in radiative recombination under high voltages is noteworthy; thus, the luminescence intensity increases with increasing voltage. It should be noted that the Auger non-radiative recombination route becomes dominant since the Auger recombination rate increases much faster than the radiative recombination rate at high voltages, which would influence the performance of LE-MOSJ devices [39]. As is well known, an increase in the electric field will enhance the infield emission rate of defect-trapped electrons. Thus, the electrons trapped by defects at the QD/Ag interface will be released faster due to the enhancement of the electric field [40]. Therefore, with increasing voltages, the EL intensity of P2 increases faster than that of P1, and the value of Δt for P2 decreases faster than that for P1.

Recently, S.-M. Jung and Jong Min Kim et al. proposed a rigorous charge transport model for comprehensively simulating the charge-carrier transport across QD-LED devices, which fully considers the effect of Auger recombination on QD-LED device performance in simulation and shows the excellent agreement between simulations and experiments [39]. If the Auger recombination and the electric-field-dependent capture process are quantitatively analyzed in the charge-carrier transport process of our LE-MOSJ devices, a more rigorous physical model of LE-MOSJ device would be proposed.

When the voltage is switched from negative to positive bias, a process similar to that described in the previous paragraph happens. The only difference is that the electrons for radiative recombination are among those that have accumulated in the Al_2O_3/QD interface. Under a positive bias (stage IV), electrons accumulate in the Al_2O_3/QD interface in an equilibrium state, as illustrated in Fig. 4(c)-IV. At the moment the voltage switches from negative to positive bias (stage V), the reversed electric field will drive those accumulated electrons towards the QD layer, and most of those electrons will move directly to the QDs where they take part in radiative recombination; this causes the first luminescence peak (P3) with large amplitude, as illustrated in Fig. 4(c)-V. However, a few electrons are captured by surface defects on the Al_2O_3/QD interface. Those captured electrons will be released gradually and be driven by an electric field (stage VI). This causes the second luminescence peak (P4), as illustrated in Fig. 4(c)-VI. Because only a small portion of those electrons are captured, P4 is weaker than P3. Similarly, more carriers are moving into the QDs under high voltages; thus, the luminescence intensity increases with increasing voltage. Also, the electrons trapped by QD/Al_2O_3 defects will be released faster due to the enhanced electric field, so with increasing voltage, P4 will increase faster than P3, and the value of Δt for P4 will decreases faster than that for P3. Note that the difference in the intensities of P2 and P4 is caused by the different defect densities between the Al_2O_3/QD and the Ag/QD interfaces. Because Ag atoms are prone to introduce defects into QDs during vapor deposition, the number of defects at the Ag/QD interface will be larger than that at the Al_2O_3/QD interface. Therefore, the EL intensity of P2 is higher than that of P4. The above explanation is consistent with the experimental results.

In applications of our LE-MOSJ array in ultrahigh-resolution displays, the size and the density of pixels must be considered. Fig. 5(a) shows the morphology of a fine-patterned LE-MOSJ array as obtained using a 3D measuring laser microscope; the height profile of the LE-MOSJ array, which exhibits clean, sharp edges, is presented in the

Table 1
A summary table with the four peaks.

EL peak	EL intensity (a.u.) @ 40 V	Δt (μs) @ 40 V	Electron source
P1	0.316	0.248	Electrons injected from Ag electrode
P2	0.597	0.982	Electrons trapped by shallow defects at Ag/QD interface
P3	0.617	0.264	Electrons accumulated at Al_2O_3/QD interface
P4	0.184	1.268	Electrons trapped by shallow defects at Al_2O_3/QD interface

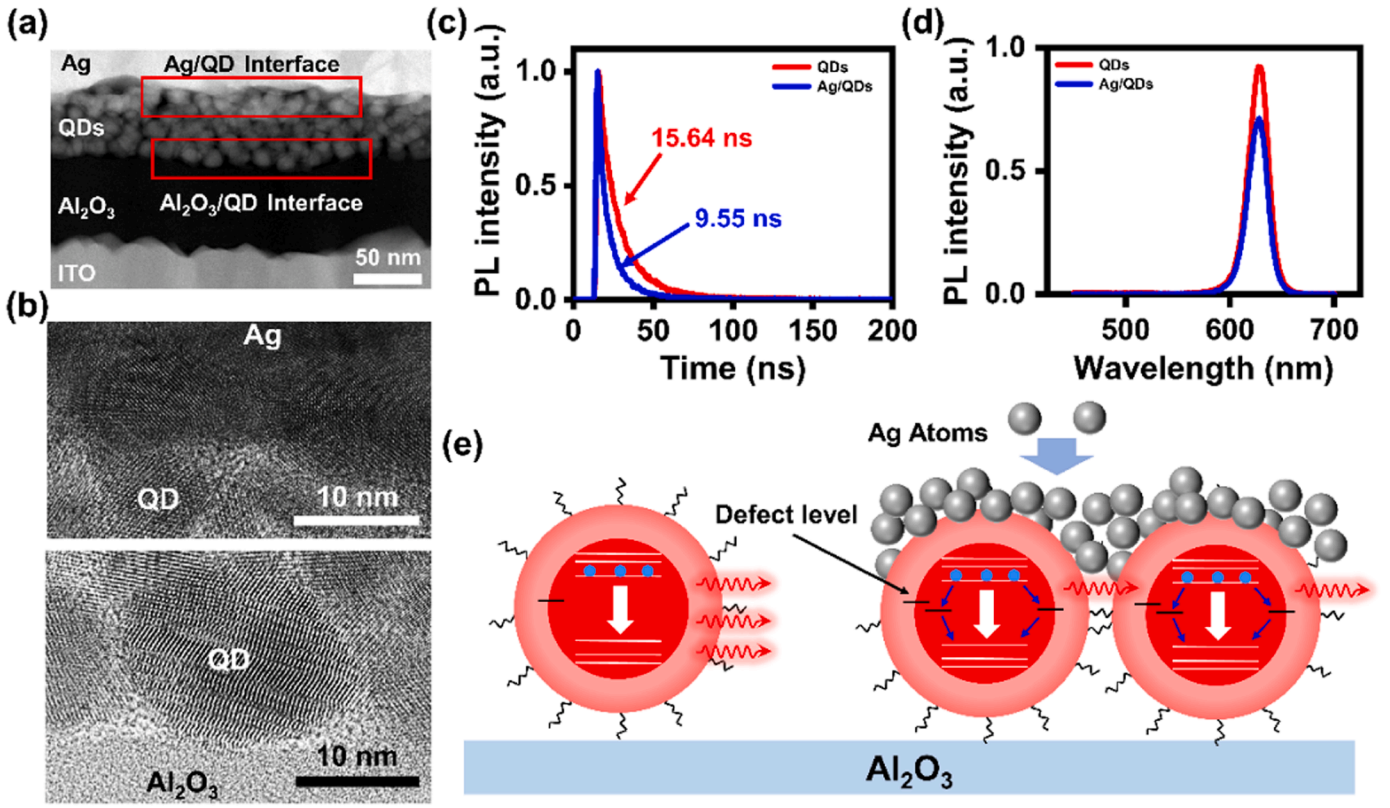

Fig. 3. Analysis of the Ag/QD and the Al_2O_3/QD interface. (a) Cross-sectional TEM image of the Ag/QDs/Al_2O_3/ITO stacking layer. (b) High magnification TEM image of the Ag/QD interface (top) and the Al_2O_3/QD interface (bottom). (c) Time-resolved photoluminescence of the QD samples with and without the Ag film. (d) PL of the QD samples with and without the Ag film. (e) Schematic diagram showing the effect of Ag deposition on the QD luminescence. The thermal evaporation of Ag introduces more defects at the Ag/QD interface.

bottom panel. The diameter of the fabricated hole is ~2.89 μm, and the pitch is ~6 μm. Fig. 5(b) depicts an EL microscope photograph of the LE-MOSJ array under a voltage of 50 V at 100 kHz; the homogeneity of the EL across all pixels can be seen. The inset image, which is a magnified view of the LE-MOSJ array, shows that the pixels have diameters of 2.89 μm, which corresponds to resolutions up to 4200 PPI and meets the requirement for ultrahigh-resolution, near-eye displays. Moreover, the distribution of the EL intensity in the inset image of Fig. 5(b) shows uniform brightness in each pixel, as presented in Fig. 5(c). A series of microscope photographs indicates good luminescence uniformity of the LE-MOSJ under different voltages from 30 V to 50 V.

Additionally, Table 2 lists the comparisons of device structure and resolution between this work and other high-resolution technologies reported previously. The LE-MOSJ devices have the advantages of the simple fabrication process and high resolution compared to other high-resolution devices reported so far.

As mentioned above, the Al_2O_3 layer can effectively suppress the transverse conductivity, allowing electrical isolation from neighboring pixels to be achieved; this is demonstrated in Fig. 5(e), which shows comparisons of the optical, PL, and EL images of two neighboring regions (region 1 and region 2). When the voltage is applied to region 1, only the LE-MOSJs in region 1 are lit, but none of the devices in region 2 are. The biased and the unbiased regions are found to have very clear luminous boundaries, which proves that no electrical interference occurs between neighboring regions in the device. Therefore, our LE-MOSJ has potential application in ultrahigh-resolution display technology.

In this work, we demonstrate the high-resolution LE-MOSJ device with a simple structure. In practical near-eye display devices, the temporally separated EL peaks have little effect on the display performance. The reason is that it is difficult for human eyes to distinguish the tiny time interval due to its short time scale (1–2 μs). Additionally, the driver technology must be considered besides the light-emitting device. Since it is difficult to reduce the pixel size of glass-based thin film transistor (TFT) driver backplane, we believe that a silicon-based CMOS driver backplane should be used for realizing practical application. Moreover, the LE-MOSJ devices can be driven by pulsed square waves, and it is feasible to use a silicon-based COMS backplane to drive our LE-MOSJ devices. However, for silicon-based CMOS driver backplane, it is difficult to achieve tens of voltage output. Therefore, in further research, it is necessary to reduce the operating voltages by optimizing the QDs layer and insulating layers, so as to match the silicon-based CMOS driver technology. The optimization of the LE-MOSJ can be performed in the following strategies: (1) The materials with high dielectric constant ε is used as the insulating layer. The capacitance C of LE-MOSJ device, which represents the ability of store charge, is described as the formula $C = \frac{\varepsilon \times S}{4\pi \times k \times d}$. Here, S is the area of LE-MOSJ QD individual pixel devices, k is electrostatic constant, and d is the distance between the two electrodes in LE-MOSJ. If adapting materials with high dielectric constant ε, the result indicates that more carrier can be injected into LE-MOSJ under the same voltage rather than other materials with low dielectric constant, which is helpful to improve the performance of LE-MOSJ device meeting miniaturization and integration requirements for near-eye displays. (2) The semiconductor materials with different treatment are used as the light-emitting layer. For example, nano-metal particles doped in the quantum dots layer would reduce the interface barrier to provide more carriers, which facilitates to meet miniaturization and integration requirements for near-eye displays.

3. Conclusion

In summary, a QD-based light-emitting metal/oxide/semiconductor junction (LE-MOSJ) with a structure of ITO/Al_2O_3/QDs/Ag is proposed

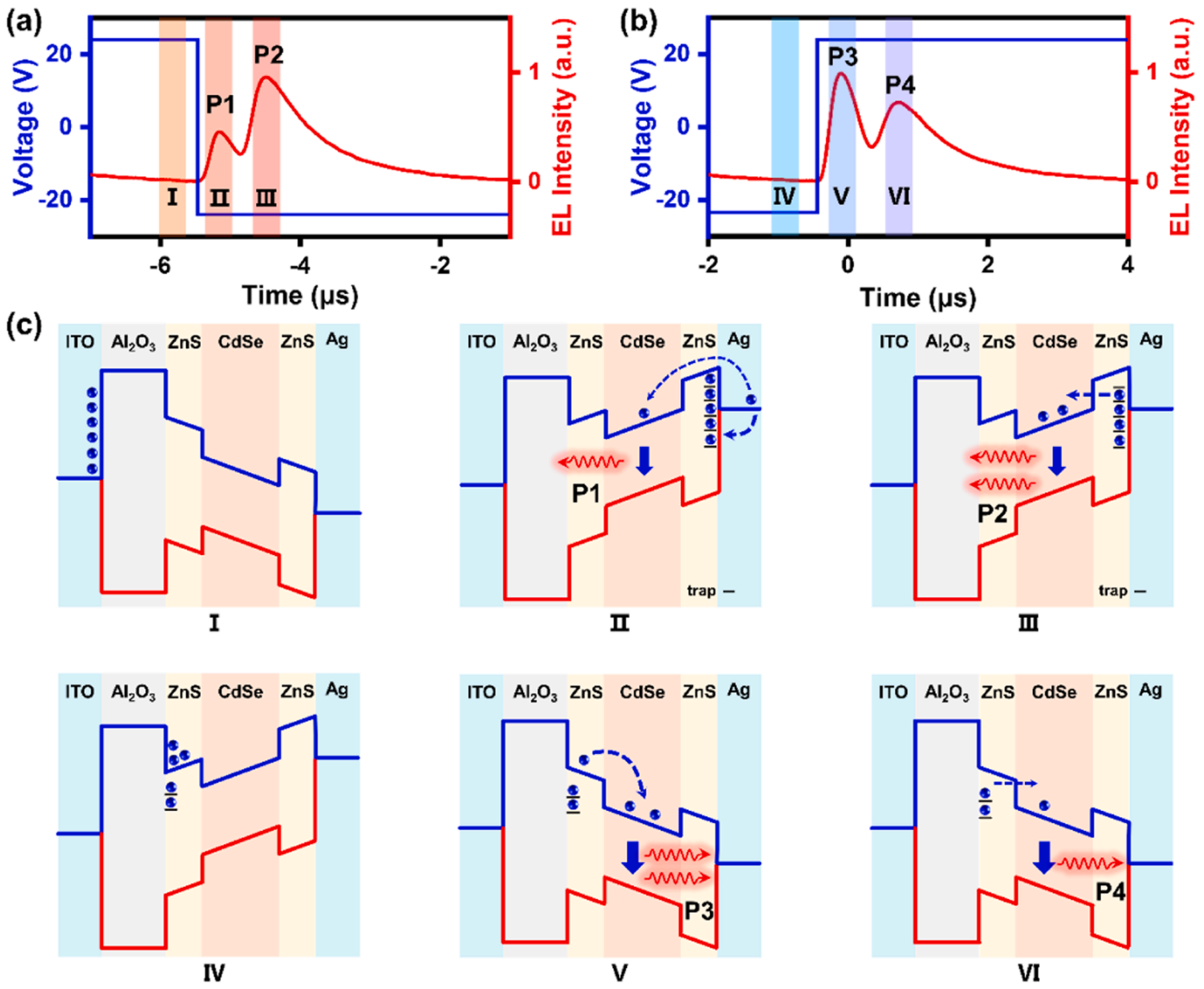

Fig. 4. Working mechanisms of the LE-MOSJ. (a) The three stages (I, II, III) when the voltage switches from positive to negative. (b) The three stages (IV, V, VI) when the voltage switches from negative to positive. (c) Schematic diagrams showing the behavior of electron transport from stage I to stage VI. Stage I: electrons accumulate in the ITO/Al_2O_3 interface in the initial state. Stage II: generation of P1. Stage III: generation of P2. Stage IV: electrons accumulate in the Al_2O_3/QD interface in an equilibrium state. Stage V: generation of P3. Stage VI: generation of P4.

for potential application in high-resolution displays. The ultra-simple structure of the LE-MOSJ avoids the need for precise vertical alignment of the functional materials and overcomes the effects of electric crosstalk in ultrahigh-resolution displays. Because of the introduction of the Al_2O_3 layer, the LE-MOSJ should be operated under an AC bias and is sensitive to the frequency of the operation voltage. A working mechanism of the alternating electroluminescence is proposed based on time-resolved electroluminescence. The electron sources for the electroluminescence are attributed to free and defect-captured electrons, which leads to two temporally separated EL peaks while the voltage polarity is switching. An LE-MOSJ array with a pixel density of 4200 PPI that can inhibit the crosstalk effect in high-resolution displays is demonstrated. The results presented in this study indicate that the LE-MOSJ can provide direction for future progress in ultrahigh-resolution light-emitting technology.

4. Experiment section

Fabrication of the LE-MOSJ: Al_2O_3 layers (60 nm in thickness) are deposited on patterned ITO electrodes by using atomic layer deposition (BENEQ, TFS 200). CdSe/ZnS QDs (25 mg/ml, Suzhou Xingshuo Nano) are spin-coated onto the ITO/Al_2O_3 substrate at a speed of 500 rpm for 5 s and then 3000 rpm for 40 s. Finally, the Ag electrodes (100 nm in thickness) are deposited by using thermal evaporation in the current of 290 A. The Ag material is purchase from ZhongNuo Advanced Material (Beijing) Technology Co., Ltd.

Fabrication of the high-resolution LE-MOSJ array: An Al_2O_3 layer (60 nm in thickness) is deposited on patterned ITO electrodes by using atomic layer deposition. Then, a positive photoresist layer (850 nm in thickness) is coated onto the Al_2O_3 layer at 500 rpm for 5 s and then 4000 rpm for 30 s, followed by baking at 90 °C for 90 s. Then, a hole array (3 μm in diameter, 6 μm in pitch) is obtained by using photolithography, followed by post baking at 120 °C for 90 s. CdSe/ZnS QDs (25 mg/ml) are spin-coated onto the patterned substrate at a speed of 500 rpm for 5 s and then 3000 rpm for 40 s. Finally, Ag electrodes (100 nm in thickness) are deposited by using thermal evaporation.

Characterizations: The fabricated devices are driven by using an alternating current (AC) voltage, which is generated using a waveform

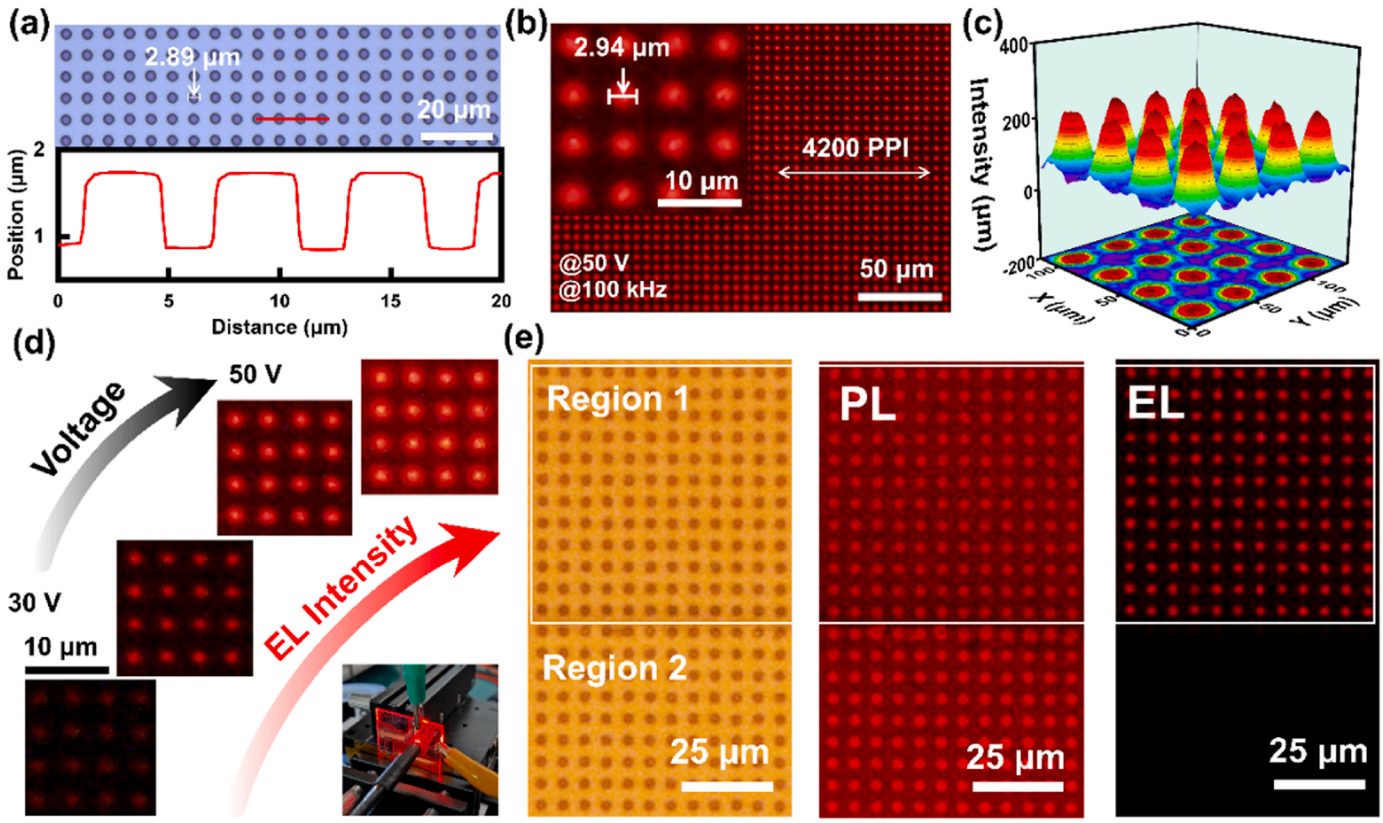

Fig. 5. Electroluminescence of the high-resolution LE-MOSJ array with a pixel density of 4200 PPI. (a) Morphology of the fine-patterned LE-MOSJ array (top) and the height profile of LE-MOSJ array corresponding to the red line in the top panel (bottom). (b) EL image of the LE-MOSJ array at 50 V and 100 kHz. The inset is a magnified image. (c) EL intensity distribution. (d) A series of microscope photographs under different voltages (from 30 V to 50 V). (e) Comparison of the optical, PL, and EL images of two neighboring regions (region 1 and region 2).

Table 2
A comparison between LE-MOSJ devices and other high-resolution technologies.

Device	Technology	Device Structure	Resolution	Reference
QLED	Photolithography	QDs/Al_2O_3	4200 PPI	This work
QLED	Electrostatic force-induced deposition	TFB/QDs/ ZnMgO	2116 PPI	[41]
QLED	Photolithography	ZnMgO/QDs/ TFB/ PEDOT:PSS	5 μm	[21]
OLED	Photolithography	PPy/NPB/ Alq_3/Liq	10 μm	[42]
QLED	Inkjet printing	ZnO/QDs/ Poly TPD/ PEDOT:PSS	500 PPI	[43]
QLED	Transfer printing	PEDOT:PSS/ TFB/QDs/ ZnMgO	9072 PPI	[23]
QLED	Intaglio transfer printing	PEDOT:PSS/ TFB/QDs/ ZnO/Li	2460 PPI	[17]
QLED	Electrohydrodynamic printing	HAT-CN/NPB/ TCTA/ QDs/ZnO	500 PPI	[19]

generator (RIGOL, DG4162) and an amplifier (Aigtek, ATA-2161). During the measurement, the bottom ITO electrode is grounded, and the voltage is applied to the top Ag electrode. The EL intensity is collected by using a luminance meter (Everfine SRC-200 M), and the time-resolved light waveforms are detected by using an avalanche photodetector (Thorlabs, APD120A2/M) and an oscilloscope (RIGOL, DS1102E). The morphology of the fine-patterned LE-MOSJ array and the height profile of the LE-MOSJ array are obtained using a 3D measuring laser microscope (OLYMPUS, OLS4100). Both TEM (FEI Titan 300) and SEM (FEI Helios 450S dual beam FIB) images are used to characterize a cross-section of the LE-MOSJ.

CRediT authorship contribution statement

Junlong Li and Jiawen Qiu contributed equally to this work. Junlong Li: contributed to data collection, formal analysis, investigation, and the writing of the original draft. Jiawen Qiu: contributed to data collection, formal analysis, and investigation. Biao Xie, Wenhao Li, Kun Wang, Chan Hee Suk, Yongshen Yu, Yun Ye: involved with the formal analysis, investigation, resources, supervision, and validation. Chaoxing Wu: involved with the conceptualization, formal analysis, investigation, project administration, resources, supervision, and validation. Yongai Zhang, Xiongtu Zhou, Tailiang Guo, Tae Whan Kim: contributed to the conceptualization, formal analysis, resources, supervision, funding acquisition and validation. All authors have read and agreed to the published version of the manuscript.

Declaration of Competing Interest

The authors declare that they have no known competing financial interests or personal relationships that could have appeared to influence the work reported in this paper.

Data Availability

Data will be made available on request.

Acknowledgements

This research was supported by grants from the National Key Research and Development Program of China (2021YFB3600400), the National Natural Science Foundation of China (62004039), the Natural Science Foundation of the Fujian Province, China (2021J01863), and the Fujian Science & Technology Innovation Laboratory for Optoelectronic Information of China Project (2020ZZ113 2021ZZ130) and by a grant from the National Research Foundation of Korea (NRF) funded by the Korea government's Ministry of Science and Technology (MSIT) (No. 2018R1A5A7025522).

References

[1] T.W. Nam, M. Kim, Y.M. Wang, G.Y. Kim, W. Choi, H. Lim, K.M. Song, M.J. Choi, D. Y. Jeon, J.C. Grossman, Y.S. Jung, Thermodynamic-driven polychromatic quantum dot patterning for light-emitting diodes beyond eye-limiting resolution, Nat. Commun. 11 (2020), 3040, https://doi.org/10.1038/s41467-020-16865-7.

[2] J. Bae, Y. Shin, H. Yoo, Y. Choi, J. Lim, D. Jeon, I. Kim, M. Han, S. Lee, Quantum dot-integrated GaN light-emitting diodes with resolution beyond the retinal limit, Nat. Commun. 13 (2022), 1862, https://doi.org/10.1038/s41467-022-29538-4.

[3] J.W. Wang, J.A. Niu, W. Sha, X.H. Dai, T.C. Huang, Q.L. Hua, Y. Long, J.F. Xiao, W. G. Hu, Flexible high-resolution micro-LED display device with integrations of transparent, conductive, and highly elastic hydrogel, Nano Res 16 (2023) 11893–11899, https://doi.org/10.1007/s12274-023-5731-x.

[4] T. Fujii, C. Kon, Y. Motoyama, K. Shimizu, T. Shimayama, T. Yamazaki, T. Kato, S. Sakai, K. Hashikaki, K. Tanaka, Y. Nakano, 4032 ppi high-resolution OLED microdisplay, J. Soc. Inf. Disp. 26 (2018) 178–186, https://doi.org/10.1002/jsid.656.

[5] Q.Q. Mu, Z.L. Cao, L.F. Hu, D.Y. Li, L. Xuan, Adaptive optics imaging system based on a high-resolution liquid crystal on silicon device, Opt. Express 14 (2006) 8013–8018, https://doi.org/10.1364/OE.14.008013.

[6] A.P. Alivisatos, Semiconductor clusters, nanocrystals, and quantum dots, Science 271 (1996) 933–937, https://doi.org/10.1126/science.271.5251.933.

[7] S. Coe, W.K. Woo, M. Bawendi, V. Bulovic, Electroluminescence from single monolayers of nanocrystals in molecular organic devices, Nature 420 (2002) 800–803, https://doi.org/10.1038/nature01217.

[8] V.L. Colvin, M.C. Schlamp, A.P. Alivisatos, Light-emitting-diodes made from cadmium selenide nanocrystals and a semiconducting polymer, Nature 370 (1994) 354–357, https://doi.org/10.1038/370354a0.

[9] K.S. Cho, E.K. Lee, W.J. Joo, E. Jang, T.H. Kim, S.J. Lee, S.J. Kwon, J.Y. Han, B. K. Kim, B.L. Choi, J.M. Kim, High-performance crosslinked colloidal quantum-dot light-emitting diodes, Nat. Photonics 3 (2009) 341–345, https://doi.org/10.1038/nphoton.2009.92.

[10] J.M. Caruge, J.E. Halpert, V. Wood, V. Bulovic, M.G. Bawendi, Colloidal quantum-dot light-emitting diodes with metal-oxide charge transport layers, Nat. Photonics 2 (2008) 247–250, https://doi.org/10.1038/nphoton.2008.34.

[11] X. Lin, X.L. Dai, C.D. Pu, Y.Z. Deng, Y. Niu, L.M. Tong, W. Fang, Y.Z. Jin, X.G. Peng, Electrically-driven single-photon sources based on colloidal quantum dots with near-optimal antibunching at room temperature, Nat. Commun. 8 (2017), 1132, https://doi.org/10.1038/s41467-017-01379-6.

[12] R. Arians, A. Gust, T. Kummell, C. Kruse, S. Zaitsev, G. Bacher, D. Hommel, Electrically driven single quantum dot emitter operating at room temperature, Appl. Phys. Lett. 93 (2008), 173506, https://doi.org/10.1063/1.3009302.

[13] P.P. Zhang, G.L. Yang, F. Li, J.B. Shi, H.Z. Zhong, Direct in situ photolithography of perovskite quantum dots based on photocatalysis of lead bromide complexes, Nat. Commun. 13 (2022) 6713, https://doi.org/10.1038/s41467-022-34453-9.

[14] W.H. Mei, Z.Q. Zhang, A.D. Zhang, D. Li, X.Y. Zhang, H.W. Wang, Z. Chen, Y.Z. Li, X.G. Li, X.G. Xu, High-resolution, full-color quantum dot light-emitting diode display fabricated via photolithography approach, Nano Res 13 (2020) 2485–2491, https://doi.org/10.1007/s12274-020-2883-9.

[15] S.Y. Liang, Y.F. Liu, Z.K. Ji, S.Y. Wang, H. Xia, H.B. Sun, High-resolution patterning of perovskite quantum dots via femtosecond laser-induced forward transfer, Nano Lett. 23 (2023) 3769–3774, https://doi.org/10.1021/acs.nanolett.3c00006.

[16] S.Y. Liang, Y.F. Liu, S.Y. Wang, H. Xia, H.B. Sun, High-resolution in situ patterning of perovskite quantum dots via femtosecond laser direct writing, Nanoscale 14 (2022) 1174–1178, https://doi.org/10.1039/d1nr07516k.

[17] M.K. Choi, J. Yang, K. Kang, D.C. Kim, C. Choi, C. Park, S.J. Kim, S.I. Chae, T. H. Kim, J.H. Kim, T. Hyeon, D.H. Kim, Wearable red-green-blue quantum dot light-emitting diode array using high-resolution intaglio transfer printing, Nat. Commun. 6 (2015) 7149, https://doi.org/10.1038/ncomms8149.

[18] B.H. Kim, M.S. Onses, J.B. Lim, S. Nam, N. Oh, H. Kim, K.J. Yu, J.W. Lee, J.H. Kim, S.K. Kang, C.H. Lee, J. Lee, J.H. Shin, N.H. Kim, C. Leal, M. Shim, J.A. Rogers, High-resolution patterns of quantum dots formed by electrohydrodynamic jet printing for light-emitting diodes, Nano Lett. 15 (2015) 969–973, https://doi.org/10.1021/nl503779e.

[19] H. Wang, Y. Zhang, Y. Liu, Z. Chen, Y. Li, X. Li, X. Xu, High-efficiency and high-resolution patterned quantum dot light emitting diodes by electrohydrodynamic printing, Nanoscale Adv. 5 (2023) 1183–1189, https://doi.org/10.1039/D2NA00862A.

[20] J. Yang, D. Hahm, K. Kim, S. Rhee, M. Lee, S. Kim, J.H. Chang, H.W. Park, J. Lim, M. Lee, H. Kim, J. Bang, H. Ahn, J.H. Cho, J. Kwak, B. Kim, C. Lee, W.K. Bae, M. S. Kang, High-resolution patterning of colloidal quantum dots via non-destructive, light-driven ligand crosslinking, Nat. Commun. 11 (2020) 2874, https://doi.org/10.1038/s41467-020-16652-4.

[21] H. Gao, Y. Qie, H. Zhao, F. Li, T. Guo, H. Hu, High-performance, high-resolution quantum dot light-emitting devices through photolithographic patterning, Org. Electron. 108 (2022), 106609, https://doi.org/10.1016/j.orgel.2022.106609.

[22] H.G. Li, Y.Q. Duan, Z.L. Shao, G.N. Zhang, H.Y. Li, Y.A. Huang, Z.P. Yin, High-resolution pixelated light emitting diodes based on electrohydrodynamic printing and coffee-ring-free quantum dot film, Adv. Mater. Technol. 5 (2020), 2000401, https://doi.org/10.1002/admt.202000401.

[23] T.T. Meng, Y.T. Zheng, D.L. Zhao, H.L. Hu, Y.B. Zhu, Z.W. Xu, S.M. Ju, J.P. Jing, X. Chen, H.J. Gao, K.Y. Yang, T.L. Guo, F.S. Li, J.P. Fan, L. Qian, Ultrahigh-resolution quantum-dot light-emitting diodes, Nat. Photonics 16 (2022) 297–303, https://doi.org/10.1038/s41566-022-00960-w.

[24] D. Hahm, J. Lim, H. Kim, J.W. Shin, S. Hwang, S. Rhee, J.H. Chang, J.H.Y. Yang, C. H. Lim, H. Jo, B. Choi, N.S. Cho, Y.S. Park, D.C. Lee, E. Hwang, S. Chung, C. M. Kang, M.S. Kang, W.K. Bae, Direct patterning of colloidal quantum dots with adaptable dual-ligand surface, Nat. Nanotechnol. 18 (2023) 419, https://doi.org/10.1038/s41565-022-01182-5.

[25] S. Pradhan, F. Di Stasio, Y. Bi, S. Gupta, S. Christodoulou, A. Stavrinadis, G. Konstantatos, High-efficiency colloidal quantum dot infrared light-emitting diodes via engineering at the supra-nanocrystalline level, Nat. Nanotechnol. 14 (2019) 72–79, https://doi.org/10.1038/s41565-018-0312-y.

[26] H.B. Shen, Q. Gao, Y.B. Zhang, Y. Lin, Q.L. Lin, Z.H. Li, L. Chen, Z.P. Zeng, X.G. Li, Y. Jia, S.J. Wang, Z.L. Du, L.S. Li, Z.Y. Zhang, Visible quantum dot light-emitting diodes with simultaneous high brightness and efficiency, Nat. Photonics 13 (2019) 192–197, https://doi.org/10.1038/s41566-019-0364-z.

[27] X.T. Chen, X.F. Lin, L.K. Zhou, S.J. Sun, R. Li, M.Y. Chen, Y.X. Yang, W.J. Hou, L. J. Wu, W.R. Cao, X. Zhang, X.L. Yan, S. Chen, Blue light-emitting diodes based on colloidal quantum dots with reduced surface-bulk coupling, Nat. Commun. 14 (2023) 284, https://doi.org/10.1038/s41467-023-35954-x.

[28] D. Braun, Crosstalk in passive matrix polymer LED displays, Synth. Met. 92 (1998) 107–113, https://doi.org/10.1016/S0379-6779(98)80099-4.

[29] K. Lai, S. Yang, P. Chen, M. Yeh, M. Liao, C. Yeh, S. Ho, Y. Chang, H. Chen, Patterned-bank-free electroluminescent quantum dot emitting array for passive-matrix QLED display, Adv. Mater. Technol. 7 (2021), 2100889, https://doi.org/10.1002/admt.202100889.

[30] H. Kang, Y. Hwang, C. Kang, J. Kim, C. Joo, J. Shin, S. Sim, H. Cho, D. Ahn, N. Cho, H. Youn, Y. An, J. Kim, C. Byun, H. Lee, Investigating the electrical crosstalk effect between pixels in high-resolution organic light-emitting diode microdisplays, Sci. Rep. 13 (2023), 14070, https://doi.org/10.1038/s41598-023-41033-4.

[31] Y.W. Shen, W.H. Li, K. Wang, R. Chen, C.X. Wu, X.T. Zhou, Y.A. Zhang, Y. Xiao, S. L. Zhao, T.L. Guo, In-well ionization from monolayer quantum dots for non-carrier-injection electroluminescence, J. Phys. Chem. Lett. 13 (2022) 10649–10655, https://doi.org/10.1021/acs.jpclett.2c02879.

[32] C. Wu, K. Wang, T. Guo, Theoretical study of led operating in noncarrier injection mode, Nanomaterials 12 (2022) 2532, https://doi.org/10.3390/nano12152532.

[33] J.B. Feng, Y.Z. Li, J.X. Zhang, Y.Q. Tang, H. Sun, L. Gan, C.Z. Ning, Injection-free multiwavelength electroluminescence devices based on monolayer semiconductors driven by an alternating field, Sci. Adv. 8 (2022), eabl5134, https://doi.org/10.1126/sciadv.abl5134.

[34] K. Wang, P.Q. Chen, J.J. Chen, Y. Liu, C.X. Wu, J. Sun, X.T. Zhou, Y.A. Zhang, T. L. Guo, Alternating current electroluminescence from GaN-based nanorod light-emitting diodes, Opt. Laser Technol. 140 (2021), 107044, https://doi.org/10.1016/j.optlastec.2021.107044.

[35] K. Wang, Y. Liu, C.X. Wu, D.L. Li, S.H. Lv, Y.G. Zhang, X.T. Zhou, T.L. Guo, Electroluminescence from mu LED without external charge injection, Sci. Rep. 10 (2020), 8059, https://doi.org/10.1038/s41598-020-65092-z.

[36] F.T. Xia, X.W. Sun, S.M. Chen, Alternating-current driven quantum-dot light-emitting diodes with high brightness, Nanoscale 11 (2019) 5231–5239, https://doi.org/10.1039/c8nr10461a.

[37] Y. Gao, X.G. Peng, Photogenerated excitons in plain core CdSe nanocrystals with unity radiative decay in single channel: the effects of surface and ligands, J. Am. Chem. Soc. 137 (2015) 4230–4235, https://doi.org/10.1021/jacs.5b01314.

[38] C.D. Pu, X.G. Peng, To battle surface traps on CdSe/CdS core/shell nanocrystals: shell isolation versus surface treatment, J. Am. Chem. Soc. 138 (2016) 8134–8142, https://doi.org/10.1021/jacs.6b02909.

[39] S.-M. Jung, T.H. Lee, S.Y. Bang, S.D. Han, D.-W. Shin, S. Lee, H.W. Choi, Y.-H. Suh, X.-B. Fan, J.-W. Jo, S. Zhan, J. Yang, C. Samarakoon, Y. Kim, L.G. Occhipinti, G. Amaratunga, J.M. Kim, Modelling charge transport and electro-optical characteristics of quantum dot light-emitting diodes, npj Comput. Mater. 7 (2021), 122, https://doi.org/10.1038/s41524-021-00591-9.

[40] S. Lee, E.H. Kim, S. Yu, H. Kim, C. Park, T.H. Park, H. Han, S.W. Lee, S. Baek, W. Jin, C.M. Koo, C. Park, Alternating-current MXene polymer light-emitting diodes, Adv. Funct. Mater. 30 (2020), 2001224, https://doi.org/10.1002/adfm.202001224.

[41] C. Luo, Z. Zheng, Y. Ding, Z. Ren, H. Shi, H. Ji, X. Zhou, Y. Chen, High-resolution, highly transparent, and efficient quantum dot light-emitting diodes, Adv. Mater. 35 (2023), 2303329, https://doi.org/10.1002/adma.202303329.

[42] J. Li, Y. Hu, X. Liang, J. Chen, L. Zhong, L. Liao, L. Jiang, H. Fuchs, W. Wang, Y. Wang, L. Chi, Micro organic light emitting diode arrays by patterned growth on structured polypyrrole, Adv. Opt. Mater. 8 (2020), 1902105, https://doi.org/10.1002/adom.201902105.

[43] P. Yang, L. Zhang, D. Kong, D. Kong, R. Strahl, T. Krause, High-resolution inkjet printing of quantum dot light-emitting microdiode arrays, Adv. Opt. Mater. 8 (2020), 1901429, https://doi.org/10.1002/adom.201901429.